Aerospace Science and Technology 112 (2021) 106592

Contents lists available at ScienceDirect

Aerospace Science and Technology

www.elsevier.com/locate/aescte

Steadiness of wave complex induced by oblique detonation wave reflection before an expansion corner

Kuanliang Wang [a], Pengfei Yang [b,c], Honghui Teng [a,*]

[a] School of Aerospace Engineering, Beijing Institute of Technology, Beijing 100081, China
[b] State Key Laboratory of High Temperature Gas Dynamics, Institute of Mechanics, Chinese Academy of Sciences, Beijing 100190, China
[c] School of Engineering Sciences, University of Chinese Academy of Sciences, Beijing 100049, China

ARTICLE INFO

Article history:
Received 27 September 2020
Received in revised form 31 January 2021
Accepted 15 February 2021
Available online 19 February 2021
Communicated by Yu Lv

Keywords:
Oblique detonation
Wave complex
Instability
Thermal choking
Expansion corner

ABSTRACT

Oblique detonation wave (ODW) reflection before an expansion corner leads to a sophisticated wave complex, whose steadiness is critical to achieve a practical oblique detonation engine. Both steady and unsteady wave complexes have been observed before, but the features of unsteady wave dynamics with related unsteadiness rules are still unclear so far. In this study, the ODW reflections before an expansion corner have been simulated using the reactive Euler equations with a two-step induction–reaction kinetic model, and the wave complex structures and dynamics have been analyzed correspondingly. Three subsonic zones have been distinguished, and their interactions were found to determine the wave complex steadiness. The main subsonic zone derives from the ODW reflection, which locates behind the Mach stem, while two other subsonic zones form due to the shock reflection downstream. The two downstream subsonic zones might travel upstream and combine with the main subsonic zone, resulting in two different unsteadiness modes. These wave complex dynamics were analyzed with respect to the deflection location, deflection angle and inflow Mach number, leading to the boundaries of combustion modes and ascertaining the rule of mode regime. Some transient phenomena related with the flow instability have been also discussed, clarifying fine flow structures further.

1. Introduction

A current frontier of aeronautic engineering is developing air-breathing propulsion systems for hypersonic aircrafts. Besides the well-known Scramjet [1,2], another ramjet based on oblique detonation wave (ODW) also attracts increasing attention in recent years [3,4]. This type of engine might be employed to develop advanced hypersonic aircrafts, benefiting from high thermal efficiency through pressure-gain combustion of detonation wave [5–7]. However, it is not easy to harness an ODW in the high-speed inflow, which needs to first clarify the structure and stability of ODW.

The ODW has traditionally been treated as an oblique shock wave (OSW) with instant heat release [8–10]. This treatment was an oversimplification, also ignoring the initiation region which found later by studies [11,12]. The initiation is achieved through the transition from an OSW, and two types of initiation wave structures, smooth and abrupt, have been observed and analyzed in depth [13–16]. Further studies [17–21] pay much attention on the ODW surface instability, illustrating the formation of fine wave structures and revealing the asymptotic growth of disturbance.

Above studies mainly use the assumption of a semi-infinite wedge. By relaxing it, a more realistic geometric confinement could be considered in several recent studies [22–25]. For instance, the ODW induced by a confined wedge is analyzed numerically and theoretically to combine the potential advantage of both ODW and the normal detonation [22,23] and a dual-angle ramp was utilized to explore the possibility of wave configuration inside the detonation combustor [24,26]. With a finite-length wedge, an expansion wave from the rear is introduced, which might quench the ODW [27,28] or changes the wave structures and instability [29–31]. Moreover, there are few works in literature on the upper wall of the flow tunnel, which limits the inflow with the wedge (lower wall) together. Theoretically, the upper wall should have an expansion corner downstream, so the supersonic flow could be accelerated directly to generate the impulse. The upper wall has been considered in [32,33], but the ODW reflects on the turning point of corner exactly, inducing an ideal flow structure similar to that without the upper wall. Our recent studies [34–38] illustrates two non-ideal realistic flow structures: when the corner locates upstream of the undisturbed surface, the interaction of expansion fan and ODW results in a post-corner recirculation zone, coupling

* Corresponding author.
E-mail address: hhteng@bit.edu.cn (H. Teng).

https://doi.org/10.1016/j.ast.2021.106592
1270-9638/

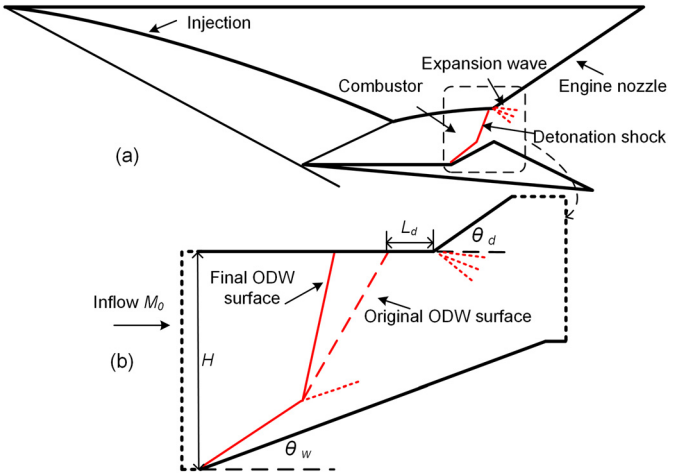

Fig. 1. Schematic of oblique detonation engine (a) and computational domain (b).

with a gaseous wedge which replaces the original expansion fan; when the corner locates upstream of the unperturbed surface, the ODW surface reflects on the upper wall, leading to a Mach stem beneath the pre-corner upper wall.

As a successive work of the ODW–wall interaction, this study investigates the wave dynamics and explores the unsteadiness features through simulating the ODW reflection on the upper wall before a corner. Previous study [35] indicates that the pre-corner ODW reflection could lead to either steady or unsteady wave complex, but it is impossible to distinguish them from the wave configurations before the thermal choking happens. Hence, this study analyzed their wave dynamics to clarify the destabilization features, through 39 cases with different M_0 and corner geometric parameters. Three possible subsonic zones have been observed, revealing two different unsteadiness modes. Furthermore, the boundaries of these steady/unsteady modes have been also plotted, and some transient phenomena have been also discussed to clarify fine flow structures.

2. Physical and numerical models

Schematic of oblique detonation engine with its main geometric parameters is shown in Fig. 1. An upper wall with an expansion corner was used to model a simplified combustor–nozzle flow. Here, L_d and θ_d are the two bifurcation parameters: L_d represents the distance along the upper wall between the deflection point and the original undisturbed ODW surface positions which was determined by the von Neumann pressure behind the shock wave; θ_d is the angle of outward deflection wall. Two other geometric parameters, H and θ_w, denote the entrance inflow height and the wedge angle, respectively. The simulation is based on the Euler equations with a two-step kinetic model to simplify chain-branching kinetics [39]. The induction reaction index ξ and heat release reaction index λ are the two key reaction variables for the transport equations

$$\frac{\partial(\rho\xi)}{\partial t}+\frac{\partial(\rho u\xi)}{\partial x}+\frac{\partial(\rho v\xi)}{\partial y} = H(1-\xi)\,\rho k_I exp\left[E_I\left(\frac{1}{Ts}-\frac{1}{T}\right)\right], \tag{2.1}$$

$$\frac{\partial(\rho\lambda)}{\partial t}+\frac{\partial(\rho u\lambda)}{\partial x}+\frac{\partial(\rho v\lambda)}{\partial y} = [1-H(1-\xi)]\,\rho(1-\lambda)\,k_R exp\left[\left(-\frac{E_R}{T}\right)\right], \tag{2.2}$$

Table 1
Chemical, gas-dynamic and geometric parameters.

Q	25
γ	1.2
E_I	$4.0T_s$
E_R	$1.0T_s$
M_0	6.5, 7.0, 7.5
θ_w	25°
θ_d	35°, 40°, 45°
H	150
L_d	1∼ 5 for M_0 = 6.5 5∼25 for M_0 = 7.0 20∼45 for M_0 = 7.5

with the Heaviside step function

$$H(1-\xi)=\begin{cases}1, & \xi\le 1,\\ 0, & \xi>1.\end{cases} \tag{2.3}$$

The equation of state should be changed to include the effects of heat release, depending on the second step index λ rather not ξ

$$e=\frac{p}{\rho(\gamma-1)}+\frac{1}{2}\left(u^2+v^2\right)-\lambda Q. \tag{2.4}$$

It should be noted that this work adopts Euler equations, although neglecting the diffusion effects may introduce some errors. As demonstrated in [14–21], almost all the previous numerical studies of ODWs assume an inviscid flow, so the Navier-Stokes equations could be simplified to be Euler equations. This is because Re, the Reynolds number, is usually very high in the ODW or other detonation works. The main error is probably derived from the boundary layer, which has been studied recently [40]. However, we estimate those simulations are still grid-dependence due to the resolution insufficiency. For our cases shown later, Re is on the scale of 10^7, so this simplification will not bring too much error. According to the boundary layer theory [41,42], the thickness near the turning point takes below 1.2% of the inflow height, but simulating it accurately will take much more computational resources. Hence, this study is performed based on Euler equations, which are solved using advection upstream splitting (AUSMPW+) [43] combined with a third-order Runge–Kutta algorithm. Flow parameters, such as pressure, density, temperature and velocities are normalized by the freestream inflow state. Initially, the whole fields are uniform with parameters calculated by M_0. The boundary conditions include the solid wall, the supersonic inflow and the supersonic outflow, which are handled by interpolation from inside.

The main parameters used in this study have been listed in Table 1. The chemical parameters are set to be the heat release amount Q = 25, specific heat capacity ratio γ = 1.2, activation energy of induction reaction E_I = $4.0T_s$, and activation energy of heat release reaction E_R = $1.0T_s$, in which T_s denotes the post-shock temperature of C–J (Chapman–Jouguet) detonation. This set of parameters does not correspond a concrete reactant, but provides a general heat release mimicking the induction–reaction kinetic process [44]. The heat release amount Q here was 25, rather not 50 like many previous studies, e.g. [39,45–47], so the corresponding C-J Mach number is about 4.5, close to that of stoichiometric hydrogen-air mixtures in standard conditions. Other parameters (γ, E_I, E_R) inherit from the previous study with no change, therefore, the typical ODW structures can be obtained with the inflow M_0 = 6.5 ∼ 7.5, which is suitable for the engine application with high altitude [48]. On the geometric parameters, the inlet height and wedge angle are constant, i.e., H = 150, θ_w = 25°, while L_d and θ_d are variable as the bifurcation parameters to investigate the effects of expansion corner. Three deflection angles larger than θ_w

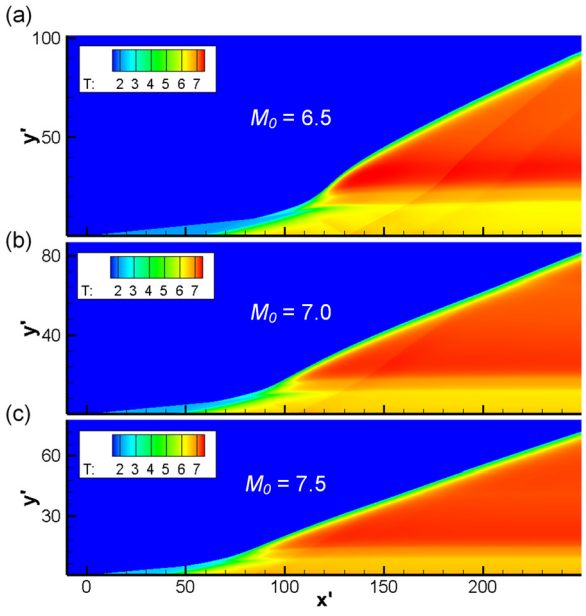

Fig. 2. ODW structure without the upper confinement in the cases of M_0 = 6.5 (a), 7.0 (b), and 7.5 (c).

(θ_d = 35°, 45°and 55°) are used to achieve a convergent-divergent flow. And the deflection location L_d changes with a different variation range according to θ_d and M_0, as shown in Table 1, so different processes could be observed and analyzed.

3. Results and discussion

3.1. Basic structures and resolution study

Three basic structures of ODW were simulated first using different M_0, as shown in Fig. 2. These structures do not consider the upper wall, so the ODW surface extends outward the upper boundary without the reflection. The obtained basic structures are all smooth transitions from the OSW to ODW, while the initiation position and the angle of ODW changes due to the variation M_0, and the first one with M_0 = 6.5 is close to the boundary between smooth transition and abrupt transition. Around the transition surface, a slip line almost parallel with the wedge manifests downstream, and the low M_0 corresponds to an obvious slip line. Previous study, such as [17], indicates that the ODW surface might be unstable, generating fine-scale wave structures, but these surfaces are stable without any wrinkles. On the whole, this structure illustrates typical ODWs with smooth transition and stable surface, whose features have been studied systematically before [35,45].

To verify the simulated results are mesh-independent, a strict resolution study has been conducted by refining the mesh in both x- and y-directions, and the results of M_0 = 7.0 case are shown in Fig. 3. The set of mesh used above use a square cell with length 0.1 along the left and upper boundaries, so the mesh number is 3000*2000. Although the cell may be distorted due to the unrectangle domain, the largest cell length remains to be smaller than 0.1. The refined mesh of resolution study uses a square cell with a length of 0.05 that the mesh number is 6000*4000 correspondingly. As shown in Fig. 3, the contours of temperature overlap together, and the quantitative evaluation of pressure/temperature profiles illustrate almost identical distributions. The mesh resolution in this work is higher than our and other researchers' previous studies, e.g. [27–30,34,40]. In addition, the set value of heat release amount (Q = 25) is relatively low, which reduces the requirement for mesh resolution. Therefore, the mesh with 3000*2000 or the

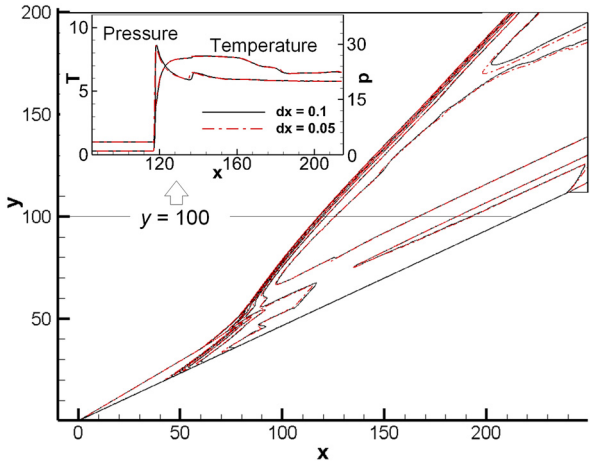

Fig. 3. Temperature fields and pressure/temperature profiles along y = 100 in the case of M_0 = 7.0.

length 0.1 is sufficient to capture the flow features, and thus used in the later simulations.

The upper deflected wall was introduced for the basic ODW in the case of M_0 = 7.0 (Fig. 2b) and leading to the structures shown in Fig. 4. As shown in Fig. 4a, when the deflection location is exactly on the wave surface by setting L_d = 0, there is almost no change in the flow field under the wall. However, by setting L_d = 10, a steady wave complex resulting from the ODW reflection on the pre-corner upper wall arises. The front of wave complex is composed of the undisturbed ODW surface and one Mach stem of ODW reflection. At the connection point of the ODW surface and Mach stem, a transverse shock extends downstream and is reflected on the wedge resulting in the RTS (reflected transverse shock), which may be further reflected on the deflected wall further. Therefore, three subsonic zones (SZs) can be observed due to multiple wave-wall reflection, as shown by black curves in Fig. 4b. It can also be found that the slip line extends downstream from the connection point, becoming unstable and causing vortex.

To facilitate the subsequent discussion, the schematic of the wave complex has been plotted in Fig. 5a and the SZs are marked one by one. The main SZ locates behind the Mach stem, which is usually the largest and plays a key role in the unsteady wave process as discussed later. The subsonic zone near the wedge (lower wall) is named as the lower SZ, while the one near the deflected upper wall is named as the upper SZ. These subsonic regions have all reached their equilibrium positions, and the entire wave complex is stable and will not change even after long enough iterations. Moreover, this wave complex arises soon when L_d increases above 0. By defining the distance between the Mach stem and expansion corner along the upper wall as L_M, the relationship between L_d and L_M can be shown Fig. 5b. A slight increase of L_d from 0 to 2 will cause a significant change in L_M, but when the L_d changes later from 2 to 10, the subsequent changes are almost linear. This demonstrates that the wave complex with Mach stem is universal, and its steadiness deserves more attention.

3.2. Effects of deflection location and angle

Based on the steady wave complex above, an unsteady one arises by increasing L_d to be 20 without changing θ_d, as shown in Fig. 6. In addition to the whole flow field, three small frames were drawn to show the evolution of unstable structures. As denoted by the time instant, the early-stage flow field at t = 294 has a similar wave complex like the last steady case. Nevertheless, the flow field then is not stationary, and causes subsequent changes in the wave locations. For the main SZ, the Mach stem travels upstream

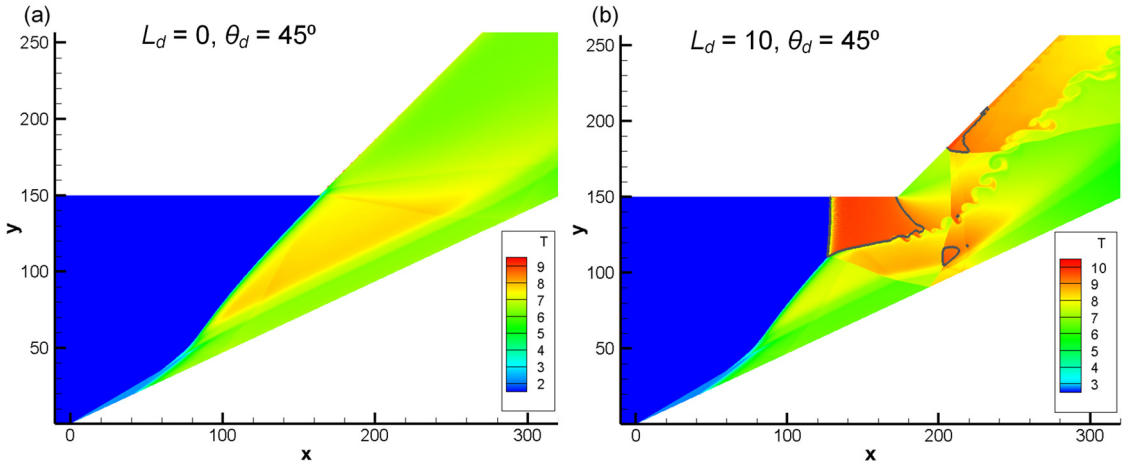

Fig. 4. Temperature fields with sonic lines (by black curves), (a) L_d = 0, θ_d = 45°, M_0 = 7.0; (b) L_d = 10, θ_d = 45°, M_0 = 7.0.

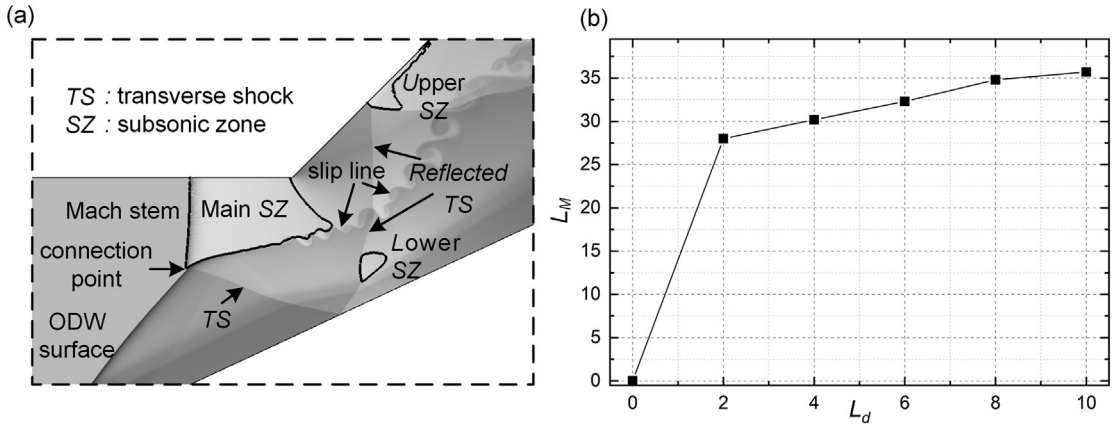

Fig. 5. (a) Schematic of wave complex induced by ODW; (b) distance between the Mach stem and expansion corner with different L_d values.

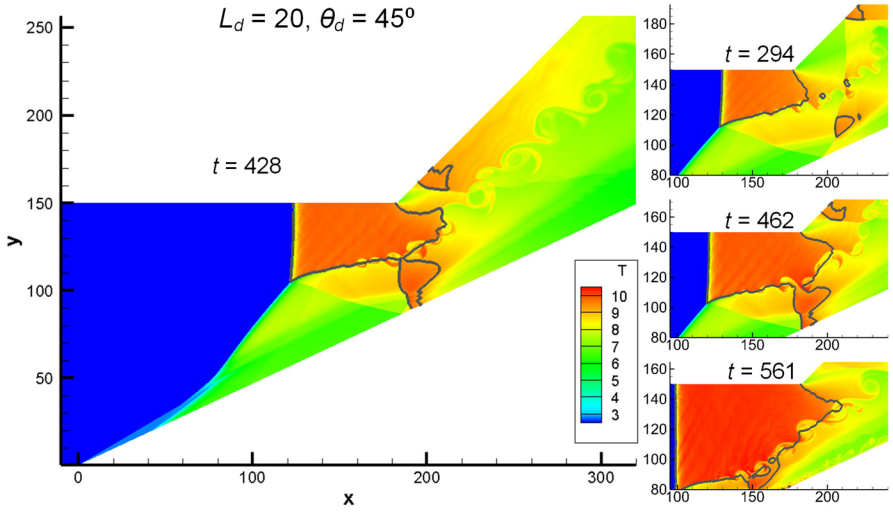

Fig. 6. Temperature fields with sonic lines (by black curves) in the cases of L_d = 20, θ_d = 45°, M_0 = 7.0.

while its rear boundary extending downstream. On the other side, both the lower and upper SZs travel upstream continuously. When t = 428, the lower SZ connects with the main SZ, as shown by the large frame of Fig. 6. The connection leads to the combination and expanding of two SZs, and triggers the thermal choke, which in turn leads to an unsteady wave complex. Generally speaking, this case demonstrates an unsteady wave complex induced by the combination of main and lower SZs, which is achieved by increasing L_d.

To study the effects of θ_d, two additional cases are simulated given θ_d = 35°or 55°. In these cases, L_d = 10 and M_0 = 7.0, corresponds a steady complex shown in Fig. 4. Numerical results demonstrate that these wave complexes are both steady, so Fig. 7 only shows the flow fields after sufficiently-long time iterations. In

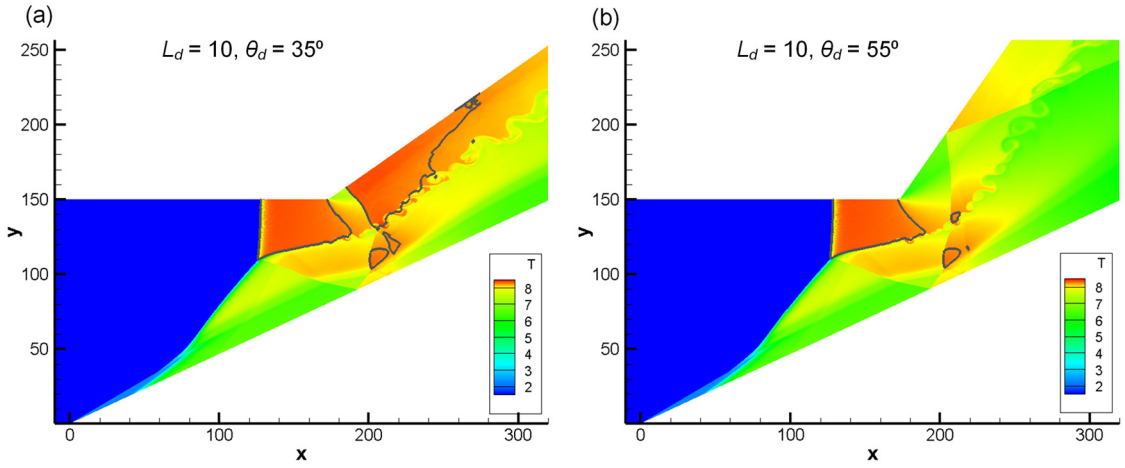

Fig. 7. Temperature fields with sonic lines (by black curves) in the cases of L_d = 10 and M_0 = 7.0, (a) θ_d = 35°; (b) θ_d = 55°.

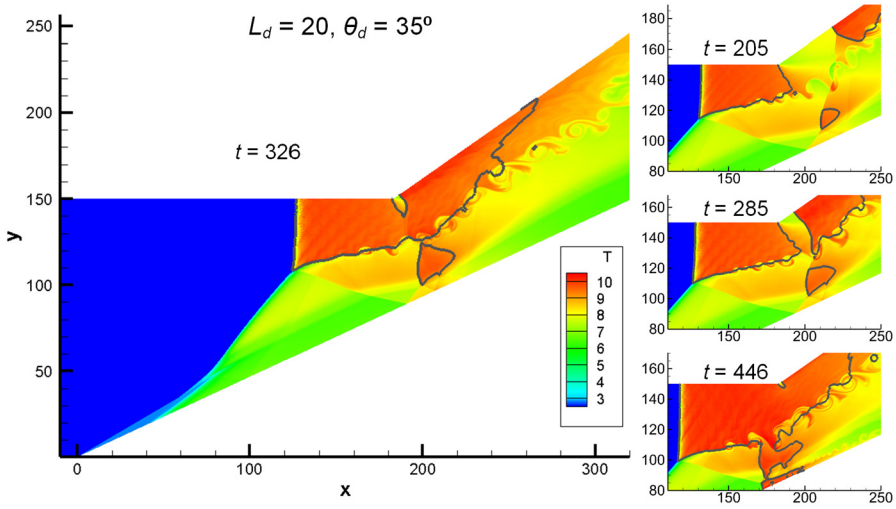

Fig. 8. Temperature fields with sonic lines (by black curves) in the case of L_d = 20, θ_d = 35°, M_0 = 7.0.

the case of θ_d = 35°, the upper SZ becomes large and very close to the rear boundary of the main SZ. This is because the expansion effect is weak with a small θ_d, then the Mach number of post-corner zone is only above 1 slightly. Hence, the wave interaction induces a large SZ, as well as the fourth SZ by interacting with the slip line near the lower SZ, as shown in Fig. 7a. In the case of θ_d = 55°, the upper SZ disappears and the lower SZ stays far away from the main SZ, with another small SZ near the slip line, as shown in Fig. 7b. On the whole, despite some differences in wave configuration, both wave complexes are stable.

By varying both L_d and θ_d together, two additional cases are investigated using L_d = 20 while θ_d = 35°or 55°. In the case of L_d = 20, θ_d = 35°, an unsteady wave complex arises whose flow dynamics are shown in Fig. 8. As shown by the small frames at t = 205 and 285, all three SZs are formed, but the upper SZ travels upstream faster than the lower SZ, which should be attributed to the low θ_d. Finally, the upper SZ instead of the lower SZ merges into the main SZ, as shown in the large frame of Fig. 8. Although the combined SZ does not choke the whole cross section then, the Mach stem travels upstream and the combined SZ expands forward and downward thereafter, leading to an unsteady wave complex. This unsteady complex is achieved by the combination of the main and upper SZs, different from that the case in Fig. 6. For the case of L_d = 20, θ_d = 55°, an unsteady complex arises through the combination of the main and lower SZs. Considering similar wave dynamics, the case with L_d = 20, θ_d = 45° is so not shown here.

Above results reveal two different wave dynamics related with unsteady complexes, one is through the combination of the main and lower SZs, while the other through the combination of the main and upper SZs. The difference of two dynamics could be distinguished from the temporal evolution of Mach stem locations, which are plotted in Fig. 9 with a steady wave complex case (L_d = 10, θ_d = 45°) plotted for reference. Clearly, the unsteady dynamics related with the lower SZ have an obvious long quasi-steady stage, denoted by green and blue curves. In contrast, the unsteady dynamics related with the upper SZ, denoted by red curves, deviates away from two other curves, indicating a different unsteady wave complex. To facilitate the subsequent discussion, the unsteady wave complex induced by the lower SZ combination with the main SZ is named as unsteady mode 1, while the other one is named as unsteady mode 2.

As mentioned above, three types of wave complex have been observed that one is steady and two are unsteady. Based on the above results, the diagram of wave complex steadiness has been plotted in Fig. 9. The complex is steady with relatively low L_d, such as with L_d = 5 or 10. Increasing L_d makes the complex unsteady, but the complex mode is determined by θ_d. The unsteady mode 1 arises in the cases of high θ_d, while the mode 2 in the cases of low θ_d. This is because the upper SZ is sensitive to θ_d, so the

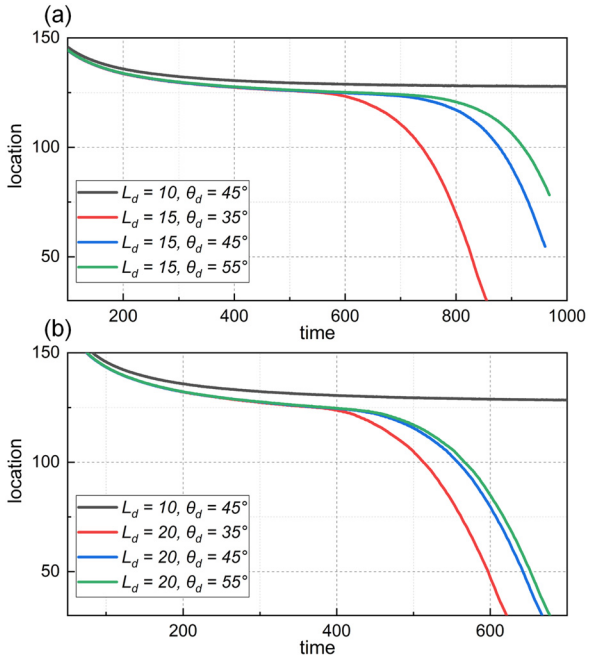

Fig. 9. Temporal location of Mach stem in different cases with M_0 = 7.0. (For interpretation of the colors in the figure(s), the reader is referred to the web version of this article.)

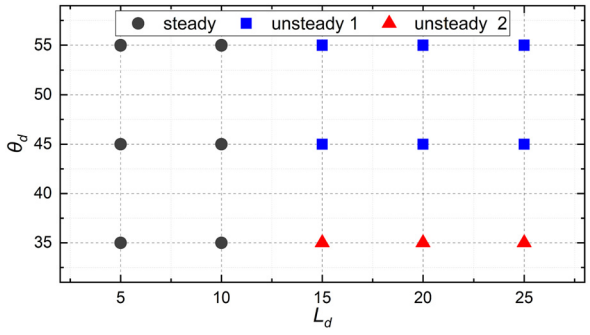

Fig. 10. Diagram of wave complex mode with M_0 = 7.0.

combination of the main and upper SZs always occurs with low θ_d, resulting in the unsteady mode 2. Simulations with a fine L_d or θ_d interval could determine more precise boundaries, but beyond the scope of this work on unsteadiness mechanisms.

3.3. Discussion on the complex features

Above 15 cases summarized in Fig. 10 are based on a fixed M_0 = 7.0. As studied before [17], the surface instability of ODWs is sensitive to M_0, and a low M_0 might induce an upstream-traveling ODW [49]. Here, we simulate the cases with M_0 = 6.5 and 7.5 to elucidate the effects of M_0 further, whose flow fields without the upper wall have been shown in Fig. 2.

Given L_d = 20, θ_d = 45°, the wave complex is unsteady in the case of M_0 = 7.0, but becomes steady in the case of M_0 = 7.5. To get an unsteady wave complex, L_d has been increased to be 30, leading to an unsteady wave complex shown in Fig. 11. In these wave dynamics, the upper SZ first combines with the main SZ, resulting in the unsteady mode 2. With M_0 = 7.5, totally 15 cases have been simulated, whose modes have been summarized in Fig. 13 and will be discussed later.

For the cases of M_0 = 6.5, the complex becomes unsteady given L_d = 10, θ_d = 45°. By decreasing L_d to be 5 or even 1, which is helpful for the steadiness according to above cases, the complex remains to be unsteady. Further studies using θ_d = 35°or 55°cannot change the complex to be steady, therefore the steady mode is absent in the cases of M_0 = 6.5. One case of the unstable wave dynamics for M_0 = 6.5 (L_d = 1, θ_d = 35°) is shown in Fig. 12. It can be observed that an unstable wave complex appears, which includes a combination of the lower and main SZs, or unstable mode 1. For each case of M_0 = 6.5, the wave complex is in unsteady mode 1.

Based on the cases with M_0 = 6.5 and 7.5, the diagram of wave complex steadiness has been plotted in Fig. 13. For the case group of M_0 = 7.5, the distribution of different modes is similar to that shown in Fig. 10, corresponding to the case group of M_0 = 7.0. Generally speaking, when L_d is low, a stable mode is generated, and when L_d is large, an unstable mode 1 is generated in the cases of high θ_d. This rule is identical to that with M_0 = 7.0, except the mode boundary variation quantitatively: increasing M_0 from 7.0 to 7.5, the steady/unsteady boundary moves toward large L_d, while the unsteady mode 1/mode 2 boundary moves toward large θ_d. However, there is still one special case, corresponding L_d = 25, θ_d = 35°, M_0 = 7.5. With the same M_0 and L_d, a large θ_d corresponds steady wave complex, but it is unsteady mode 2, suggesting the regime boundary might be not as regular as the observed ones in this study using fine parametric intervals.

For the case group of M_0 = 6.5, all the cases are unsteady mode 1, while for cases with M_0 = 7.0 and 7.5 all three modes can be generated. According to the mode regime of M_0 = 7.0 and 7.5, we try to get the unsteady mode 2 of M_0 = 6.5 by decreasing the value of θ_d and L_d, but both trails does not success finally. As shown by the flow dynamics in Fig. 11, the combination of the main and lower SZs happens soon, so there are no other steadiness modes. From the viewpoint of the mode regime, these cases could be explained by M_0 decreasing from 7.0 to 6.5: the steady/unsteady boundary moves to L_d = 0 or less, and the unsteady mode 1/mode 2 boundary moves below θ_d = 35°. Therefore, for the case group of M_0 = 6.5, the solo-steady (L_d = 0) mode is not inconsistent with other case groups with M_0 = 7.0 and 7.5, and the rule of mode regime for all three case groups is the same.

3.4. Discussion on the unstable phenomena

Besides the steadiness of wave complex discussed above, three phenomena related with flow instability have been observed and analyzed briefly here. The first one is the surface instability of Mach stem, and from the flow fields shown in Figs. 5–8, 11, and 12, an unstable Mach stem with very fine structures could be observed. The intervals of these fine structures are much less than the width of the corresponding cellular structures, with very weak transverse waves. To clarify its mechanism, further resolution studies are conducted by simulating the case with M_0 = 7, L_d = 10, θ_d = 45°, in which the lower and left boundary lengths are set to be 360 and 150, respectively. Local temperature fields with different grid resolution are displayed in Fig. 14, and the estimated mesh number on the Mach stem varies between around 150 and around 600. Obviously, the fine structures still exist regardless of the mesh length scale, and become more with a fine mesh set. Considering the Mach stem is essentially an overdriven normal detonation, the 2D overdriven detonation in the tube was also simulated and the similar local structures appeared. These tests suggest that these fine structures derive from the destabilization of normal detonation fronts at the initial stage. Some similar fine structures have been summarized before [50], but not in the ODW-induced flow fields.

The second instability phenomenon observed widely is the unstable slip line derived from the connection point. In almost each figure of flow fields, the vortex rolling induced by unstable slip line can be observed, whose mechanism should be attributed to Kelvin–Helmholtz instability (KHI). Because the unstable slip line

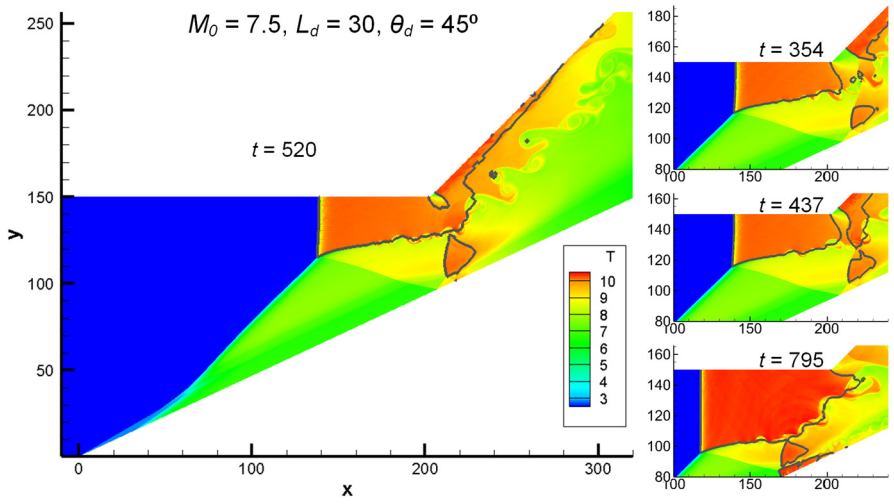

Fig. 11. Temperature fields with sonic lines (by black curves) in the case of L_d = 30, θ_d = 45°, M_0 = 7.5.

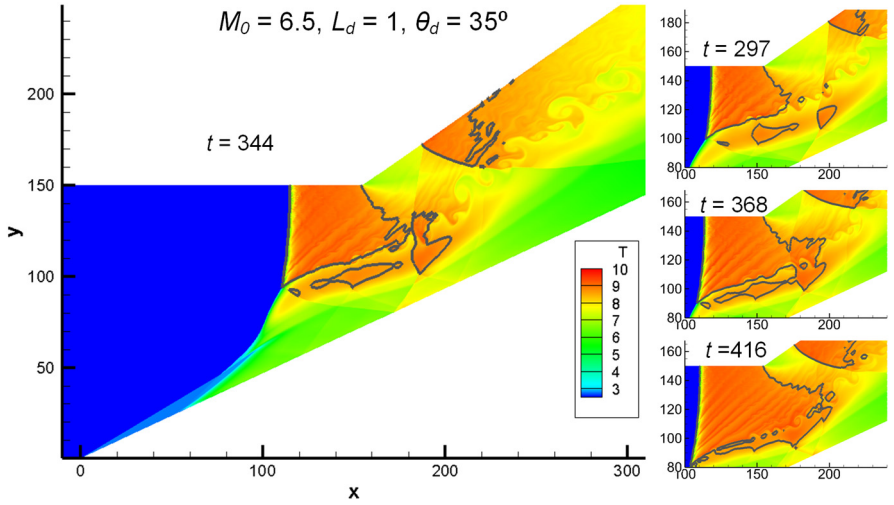

Fig. 12. Temperature fields with sonic lines (by black curves) in the case of L_d = 1, θ_d = 35°, M_0 = 6.5.

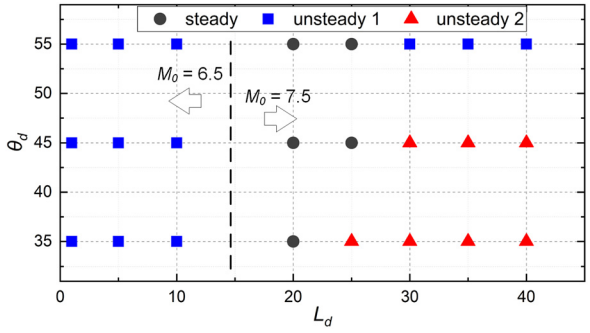

Fig. 13. Diagram of wave complex mode with M_0 = 6.5 and 7.5.

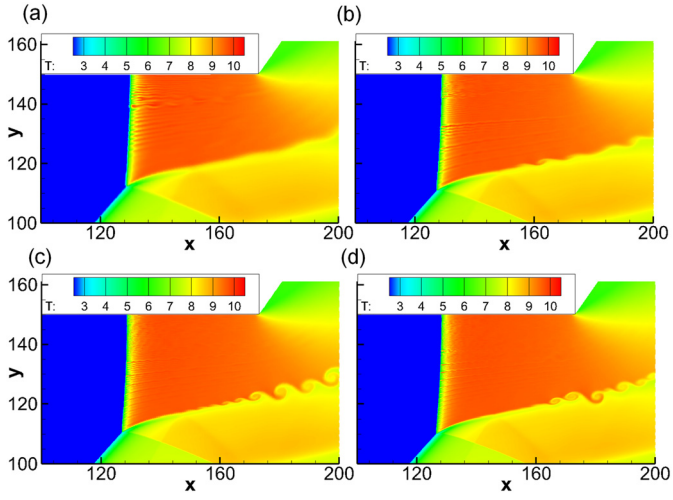

Fig. 14. Local temperature fields in the case of M_0 = 7, L_d = 10, θ_d = 45°, a fixed domain 360×150 using different mesh numbers: (a) 900×375; (b) 1800×750; (c) 2700×1000; (d) 3600×1500.

of flow fields is transient that irrelevant with the focus of this work, this evolution is not analyzed here. The third instability phenomenon is some transient streaks observed in the main SZ, but only appearing in some figures, such as Figs. 6 and 8. These streaks are featured by high temperature, which extend from left–bottom to right–up direction. However, these streaks are not observable in the wave complexes of steady mode. From the streak direction, it is deduced that the streaks might be triggered by the unstable slip line or the Mach stem movement. Hence, we revisit the initial stage of a case of steady mode (Fig. 4b), illustrating a serial of temperature gradient (along $y-$ axis direction) fields in Fig. 15. The streaks appear in the early stage, but locate before the rolling vortex. Therefore, it could be concluded that the streaks are origi-

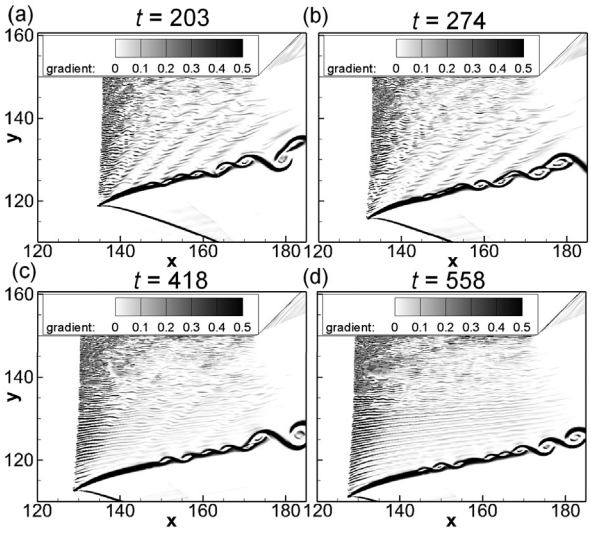

Fig. 15. Temperature gradient along y-axis direction in the cases of M_0 = 7.0, L_d = 10, θ_d = 45°.

nated from the Mach stem movement, rather not the unstable slip line.

4. Conclusion

The wave dynamic features and the unsteadiness rules in the cases of the ODW reflection before an expansion corner have been investigated in this study. Numerical results show that a sophisticated wave complex appears, the front part of which is composed of an undisturbed ODW surface and a Mach stem by the ODW reflection. Three possible subsonic zones have been observed, and their interactions determine the wave complex steadiness. The main SZ derives from the ODW reflection, while the lower/upper SZ forms due to the shock reflection downstream. The downstream lower or upper SZ might travel upstream to disturb the main SZ, and then leads to an unsteady wave complex. Two different unsteadiness modes have been distinguished, depending on which downstream SZ merges with the main SZ first. These wave complex dynamics were analyzed with respect to the deflection location, deflection angle and inflow Mach number, thereby plotting the boundaries of each mode and giving the rule of mode regime. Moreover, three transient phenomena related with the flow instability have been also observed, which are fine-scale cellular Mach stem, the unstable slip line, and the streaks inside the main SZ. Their formations are discussed and analyzed, clarifying the fine flow structures further.

Declaration of competing interest

The authors declare that they have no known competing financial interests or personal relationships that could have appeared to influence the work reported in this paper.

Acknowledgements

This research was supported by The National Natural Science Foundation of China (NSFC) (Nos. 11822202, 12002041).

References

[1] J. Urzay, Supersonic combustion in air-breathing propulsion systems for hypersonic flight, Annu. Rev. Fluid Mech. 50 (2018) 593–627.
[2] T. Vanyai, M. Bricalli, S. Brieschenk, R.R. Boyce, Scramjet performance for ideal combustion processes, Aerosp. Sci. Technol. 75 (2018) 215–226.
[3] J.Z. Ma, S. Zhang, M. Luan, et al., Experimental investigation on delay time phenomenon in rotating detonation engine, Aerosp. Sci. Technol. 88 (2019) 395–404.
[4] Z.J. Zhang, K.F. Ma, W.S. Zhang, et al., Numerical investigation of a Mach 9 oblique detonation engine with fuel pre-injection, Aerosp. Sci. Technol. 105 (2020) 1–9.
[5] J. Cheng, B. Zhang, H. Liu, F. Wang, Experimental study on the effects of different fluidic jets on the acceleration of deflagration prior its transition to detonation, Aerosp. Sci. Technol. 106 (2020) 106203.
[6] J.T. Peace, F.K. Lu, Performance modeling of pulse detonation engines using the method of characteristics, Aerosp. Sci. Technol. 88 (2019) 51–64.
[7] B. Zhang, X. Chang, C. Bai, End-wall ignition of methane-air mixtures under the effects of CO2/Ar/N2 fluidic jets, Fuel 270 (2020) 117485.
[8] R. Gross, Oblique detonation waves, AIAA J. 1 (1963) 1225–1227.
[9] D.T. Pratt, J.W. Humphrey, D.E. Glenn, Morphology of standing oblique detonation waves, J. Propuls. Power 7 (1991) 837–845.
[10] B. Zhang, H. Liu, Theoretical prediction model and experimental investigation of detonation limits in combustible gaseous mixtures, Fuel 258 (2019) 116132.
[11] C. Li, K. Kailasanath, E.S. Oran, Detonation structures behind oblique shocks, Phys. Fluids 6 (1994) 1600–1611.
[12] L.F. Figueira da Silva, B. Deshaies, Stabilization of an oblique detonation wave by a wedge: a parametric numerical study, Combust. Flame 121 (2000) 152–166.
[13] C. Viguier, L.F.F.D. Silva, D. Desbordes, B. Deshaies, Onset of oblique detonation waves: comparison between experimental and numerical results for hydrogen-air mixtures, Symp. (Int.) Combust. 26 (1996) 3023–3031.
[14] H.H. Teng, Z.L. Jiang, On the transition pattern of the oblique detonation structure, J. Fluid Mech. 713 (2012) 659–669.
[15] Y.S. Fang, Z.J. Zhang, Z.M. Hu, X. Deng, Initiation of oblique detonation waves induced by a blunt wedge in stoichiometric hydrogen-air mixtures, Aerosp. Sci. Technol. 62 (2019) 676–684.
[16] L. Yang, L.J. Yue, Q.F. Zhang, et al., Numerical study on the shock/combustion interaction of oblique detonation waves, Aerosp. Sci. Technol. 104 (2020) 1–13.
[17] J.Y. Choi, D.W. Kim, I.-S. Jeung, F. Ma, V. Yang, Cell-like structure of unstable oblique detonation wave from high-resolution numerical simulation, Proc. Combust. Inst. 31 (2007) 2473–2480.
[18] H.H. Teng, Z.L. Jiang, H.D. Ng, Numerical study on unstable surfaces of oblique detonations, J. Fluid Mech. 744 (2014) 111–128.
[19] Y.N. Zhang, J.S. Gong, T. Wang, Numerical study on initiation of oblique detonations in hydrogen–air mixtures with various equivalence ratios, Aerosp. Sci. Technol. 49 (2016) 130–134.
[20] B. Zhang, H. Liu, Y. Li, The effect of instability of detonation on the propagation modes near the limits in typical combustible mixtures, Fuel 253 (2019) 305–310.
[21] B. Zhang, H. Liu, B.J. Yan, Velocity behavior downstream of perforated plates with large blockage ratio for unstable and stable detonations, Aerosp. Sci. Technol. 86 (2019) 236–243.
[22] F.K. Lu, H.Y. Fan, D.R. Wilson, Detonation waves induced by a confined wedge, Aerosp. Sci. Technol. 10 (2006) 679–685.
[23] H.Y. Fan, F.K. Lu, Numerical modelling of oblique shock and detonation waves induced in a wedged channel, Proc. Inst. Mech. Eng., G J. Aerosp. Eng. 222 (2008) 687–703.
[24] S. Bhattrai, H. Tang, Formation of near-Chapman–Jouguet oblique detonation wave over a dual-angle ramp, Aerosp. Sci. Technol. 63 (2017) 1–8.
[25] G.X. Xiang, H.Y. Li, R.H. Cao, X.P. Chen, Study of the features of oblique detonation induced by a finite wedge in hydrogen-air mixtures with varying equivalence ratios, Fuel 264 (2020) 116854.
[26] S. Bhattrai, J.H.S. de Baar, A.J. Neely, Efficient uncertainty quantification for a hypersonic trailing-edge flap, using gradient-enhanced kriging, Aerosp. Sci. Technol. 80 (2018) 261–268.
[27] M.V. Papalexandris, A numerical study of wedge-induced detonations, Combust. Flame 120 (2000) 526–538.
[28] G. Xiang, X. Li, X. Sun, X. Chen, Investigations on oblique detonations induced by a finite wedge in high altitude, Aerosp. Sci. Technol. 95 (2019) 105451.
[29] J.Y. Choi, J.R. Shin, I.S. Jeung, Unstable combustion induced by oblique shock waves at the non-attaching condition of the oblique detonation wave, Proc. Combust. Inst. 32 (2009) 2387–2396.
[30] Y. Liu, X. Han, S. Yao, J. Wang, A numerical investigation of the prompt oblique detonation wave sustained by a finite-length wedge, Shock Waves 26 (2016) 729–739.
[31] G.X. Xiang, X. Gao, W.J. Tang, X.Z. Jie, X. Huang, Numerical study on transition structures of oblique detonations with expansion wave from finite-length cowl, Phys. Fluids 32 (2020) 056108.
[32] R. Dudebout, J.P. Sislian, R. Oppitz, Numerical simulation of hypersonic shock-induced combustion ramjets, J. Propuls. Power 14 (1998) 869–879.
[33] J. Sislian, R. Dudebout, H. Schirmer, J. Schumacher, Propulsive performance of hypersonic oblique detonation wave and shock-induced combustion ramjets, J. Propuls. Power 17 (2001) 599–604.
[34] K. Wang, H. Teng, P. Yang, H.D. Ng, Numerical investigation of flow structures resulting from the interaction between an oblique detonation wave and an upper expansion corner, J. Fluid Mech. 903 (2020) A28.

[35] K. Wang, Z. Zhang, P. Yang, H. Teng, Numerical study on reflection of an oblique detonation wave on an outward turning wall, Phys. Fluids 32 (2020) 046101.
[36] G. Zhang, G. Li, K. Wang, Wave structure of oblique detonation disturbed by an expansion wave from a bended tunnel, Appl. Them. Eng. 180 (2020) 115856.
[37] H.H. Teng, Z.L. Jiang, Progress in multi-wave structure and stability of oblique detonations, Adv. Mech. 50 (2020) 202000 (in Chinese).
[38] H.H. Teng, P.F. Yang, Y.N. Zhang, L. Zhou, Flow and combustion mechanism of oblique detonation engines, Sci. Sin. Phys., Mech. Astron. 50 (2020) 090008 (in Chinese).
[39] H.D. Ng, M.I. Radulescu, A.J. Higgins, N. Nikiforakis, J.H.S. Lee, Numerical investigation of the instability for one-dimensional Chapman–Jouguet detonations with chain-branching kinetics, Combust. Theory Model. 9 (2005) 385–401.
[40] Y. Fang, Z. Zhang, Z. Hu, Effects of boundary layer on wedge-induced oblique detonation structures in hydrogen-air mixtures, Int. J. Hydrog. Energy 44 (2019) 23429–23435.
[41] H. Schlichting, Boundary-Layer Theory, 7th ed., McGraw Hill, New York, U.S.A., 1979, p. 638.
[42] D.J. Acheson, Elementary Fluid Dynamics, second edition, Oxford Applied Mathematics and Computing Science Series, Clarendon Press, Oxford, U.K., 1992.
[43] K.H. Kim, C. Kim, O.H. Rho, Methods for the accurate computations of hypersonic flows: I. AUSMPW + scheme, J. Comput. Phys. 174 (2001) 38–90.
[44] M. Short, G.J. Sharpe, Pulsating instability of detonations with a two-step chain-branching reaction model: theory and numerics, Combust. Theory Model. 7 (2003) 401–416.
[45] H. Teng, H.D. Ng, L. Kang, C. Luo, Z. Jiang, Evolution of cellular structures on oblique detonation surfaces, Combust. Flame 162 (2015) 470–477.
[46] L. He, J.H.S. Lee, The dynamical limit of one-dimensional detonations, Phys. Fluids 7 (1995) 1151–1158.
[47] G.J. Sharpe, S.A.E.G. Falle, One-dimensional numerical simulations of idealized detonations, Proc. R. Soc. Lond. 455 (1999) 1203–1214.
[48] T. Wang, Y. Zhang, H. Teng, Z. Jiang, H.D. Ng, Numerical study of oblique detonation wave initiation in a stoichiometric hydrogen-air mixture, Phys. Fluids 27 (2015) 096101.
[49] H. Teng, Y. Zhang, Z. Jiang, Numerical investigation on the induction zone structure of the oblique detonation waves, Comput. Fluids 95 (2014) 127–131.
[50] J.H.S. Lee, Detonation Phenomena, Cambridge University Press, New York, 2008.